ACS APPLIED MATERIALS & INTERFACES

Research Article

www.acsami.org

Fabrication of a Novel Polymer-Free Nanostructured Drug-Eluting Coating for Cardiovascular Stents

Yao Wang,[†,§] Wenli Zhang,[‡,§] Jixi Zhang,[†] Wei Sun,[†] Ruiyan Zhang,*[,‡] and Hongchen Gu*[,†]

[†]Nano Biomedical Research center, School of Biomedical Engineering and Med-X Research Institute, Shanghai Jiao Tong University, Shanghai 200030, China

[‡]Department of Cardiology, Rui Jin Hospital, School of Medicine, Shanghai Jiao Tong University, Shanghai 200025, China

Supporting Information

ABSTRACT: Angioplasty with stents is the most important method for the treatment of coronary artery disease (CAD). However, the drug-eluting stents (DES) that are widely used have the increased risks of inflammatory reactions and late stent thrombosis (LST) because of the persistence of the polymer coatings. To improve the biosafety, a novel polymer-free-composite drug-eluting coating composed of magnetic mesoporous silica nanoparticles (MMSNs) and carbon nanotubes (CNTs) was constructed using the electrophoretic deposition (EPD) method in this study. A crack-free two-layered coating with impressive network nanotopologies was successfully obtained by regulating the composition and structures. This nanostructured coating exhibits excellent mechanical flexibility and blood compatibility in vitro, and the drug-loading and release performance is satisfactory as well. The in vivo study shows that this composite coating has the obvious advantage of rapid endothelialization because of its unique 3D nanostructured topology in comparison with the commercial polymer-coated DES. This study aims to provide new ideas and reliable data to design novel functional coatings that could accelerate the re-endothelialization process and avoid inflammatory reactions, thus improving the in vivo biosafety of DES.

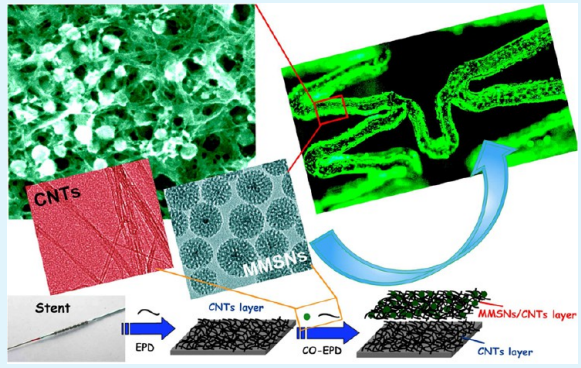

KEYWORDS: *drug-eluting stents, mesoporous silica nanoparticles, carbon nanotubes, electrophoretic deposition, re-endothelialization*

1. INTRODUCTION

Coronary artery disease (CAD) continues to be one of the leading causes of death in the world. A great revolution occurred in the late 1980s when metallic cardiovascular stents were introduced for the treatment of CAD.[1] Despite the clinical benefits, it still remains a significant challenge that 20−30% in-stent restenosis (ISR) occurs followed by the proliferation of smooth muscle cells (SMCs) in response to the mechanical injury after stenting.[2−5] Fortunately, drug-eluting stents (DES) have brought another huge leap for interventional cardiology by lowering the ISR rates to the single digits during the past decade.[6] DES carry effective antirestenotic drugs, such as rapamycin (RAPA, also named sirolimus), paclitaxel, or everolimus,[7−9] by mixing them within an organic polymer coating on the surface of stents for storage and delivery. The drugs applied for the local pharmacotherapy are directed against the proliferation of SMCs, which is the main cause of ISR.[8]

While solving the problem of ISR, a new significant issue for DES found in recent years is the increased risks of late stent thrombosis (LST) because of delayed vessel-wall healing.[10−13] A large number of reports have pointed out that it is the failure of rapid endothelialization and the persistence of non-degradable polymers that mainly result in the high risk for LST.[10,11,14−16] Unfortunately, almost all of the polymers have proinflammatory properties.[8,11,17] Biodegradable polymer coatings are being considered and investigated.[18] In spite of some promising preliminary results,[19−21] the side effects of the inflammatory reactions caused by the degradation products, such as the accumulated acids, initiators, and catalysts, have to be solved.[3,18]

Because of the drawbacks of polymer coatings mentioned above, some nonpolymer coating strategies have been employed to improve biosafety. An interesting DES platform without the obligate need for polymers created micropores on a stent as drug reservoirs through mechanical treatment.[22,23] Those micropores are beneficail for drug-loading; however, when considering that sirolimus is spray-coated onto this porous stent, after the rapid drug release the bare stent remains, posing a high risk of metal-ion release, which can lead to inflammatory reactions.[3] Similarly, nanoporous DES was also attempted previously by the introduction of a nanoporous aluminum oxide (Al_2O_3) coating,[24,25] which improved biocompatibility by means of the inert ceramic surface. However,

Received: August 12, 2013
Accepted: September 25, 2013
Published: September 25, 2013

disappointing results from an animal study were reported that indicated that particle-debris shedding from this coating led to increased vascular inflammation.[26] The combination of a stainless steel platform with a nanothin microporous hydroxyapatite (HAp) coating is another attractive attempt.[27] Impregnated with only a small amount of sirolimus, this DES system has shown promising results in an initial 1 year clinical trial.[28] Although it is probably the most excellent outcome among the polymer-free strategies at present, a meaningful concern is still raised by a recent review that suggested that big challenges will be faced after implantation to ensure the durability and integrity of these ceramic coatings.[18] Despite numerous efforts, it seems that designing new components or structured coatings is still needed for DES. In collaboration with emerging nanotechnology, coating inorganic materials, especially nanoporous, onto stents will be a promising research direction in the future.[3,18,29]

As one of the prominent representatives, mesoporous silica nanoparticles (MSNs) have been regarded as an excellent drug-carrier candidate owing to their tunable pore size, high specific surface area, large pore volume, and favorable biocompatibility.[30−33] Our group has employed core−shell-structured magnetic mesoporous silica nanoparticles (MMSNs), a family member of MSNs, as effective rapamycin-loading vehicles previously.[34−36] To the best of our knowledge, there has been no report on the assembly of MMSNs or other relatives onto implants, including cardiovascular stents, for in vivo use. Considering the inherent mechanical shortages of inorganic materials, some reinforcing elements should be incorporated into the coatings to improve their flexibility, especially for those that undergo a harsh expansion process. Carbon nanotubes (CNTs) are nanomaterials with unique 1D tubular structures. They possess a high aspect ratio and an impressive thermal and electrical conductivity as well as outstanding mechanical properties, presenting new opportunities for biomedical applications.[37−40] In addition, there is already available data suggesting that nanostructured surfaces have positive effects on cell attachment and proliferation in comparison with conventional (microstructured) ones.[41−43] Thus, constructing a 3D nanotopographical coating by assembling MMSNs and CNTs on stents might have great potential for accelerating endothelialization, which is of significant importance to reduce the risk of LST.

Herein, we utilize the electrophoretic deposition (EPD) method[44] to explore the possibility of fabricating uniform MMSNs/CNTs composite coatings on bare 316L stainless steel metal stents (316L-BMS). The study protocol is represented in Figure 1 (the details are described further in the Experimental Section). A crack-free two-layered coating was obtained by regulating the composition and structures, and the unique 3D nanotopologies are impressive. A possible mechanism for assembling the MMSNs/CNTs composite coatings is proposed as well. The integrity after expansion, the blood compatibility, and the RAPA loading and release performance of these polymer-free coatings were evaluated in vitro. Finally, the rate of re-endothelialization for the MMSNs/CNTs-coated DES was compared with the commercial polymer-coated ones by an in vivo study.

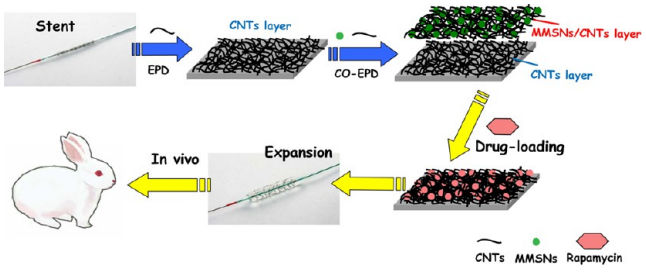

Figure 1. Schematic illustration of the strategy and route adopted for this study.

2. EXPERIMENTAL SECTION

Materials. All reagent-grade chemicals were used as received, and Millipore water (18.2 MΩ cm) was used in the preparation of all aqueous solutions. Tetraethyl orthosilicate (TEOS, AR) and ammonium nitrate (NH_4NO_3, AR) were purchased from Aladdin. Cetyltrimethylammonium bromide (CTAB, AR), sodium hydroxide (NaOH, AR), ethyl acetate (AR), absolute ethanol (AR), magnesium nitrate ($Mg(NO_3)_2{\cdot}6H_2O$, AR), and toluene (HPLC) were purchased from Sinopharm Chemical Reagent Co., Ltd., China. Magnetic mesoporous silica nanoparticles (MMSNs) were synthesized according to our previously published work (the detailed procedures can be found in the Supporting Information).[45] Carboxylated single-wall carbon nanotubes (CNTs, purity >90%) were obtained from Chengdu Organic Chemicals Co., Ltd., China. Rapamycin (RAPA), bare 316L stainless steel metal stents (316L-BMS), and commercial poly(styrene-block-isobutylene-block-styrene) (SIBS)-coated RAPA-eluting Firebird-II stents (P-FBII DES) were kindly provided by MicroPort Co., Ltd. (Shanghai, China).

Preparation of the Two-Layered CNTs@MMSNs/CNTs Composite Coatings. According to the description shown in Figure 1, the two-layered composite coatings were fabricated by two steps. That is, a thin CNTs film was first assembled onto 316L-BMS as the inner layer, and a MMSNs/CNTs coating was constructed subsequently as the second layer.

For the preparation of the inner CNTs layer, CNTs (0.6 mg) were added into an ethanol solution (10 mL) of $Mg(NO_3)_2{\cdot}6H_2O$ (1 mM). After ultrasonic treatment for 10 min, CNTs that adsorbed adequate magnesium ions were well dispersed in ethanol, and the solution was utilized for the EPD process. A cylindrical 316L stainless steel tube of 25 mm ×40 mm × 0.12 mm (diameter × height × thickness) was washed with ethanol and served as the anode. A stent (316L-BMS) was placed coaxially as the cathode for deposition. Both electrodes were immersed into the EPD bath and connected to a dc power supply. The EPD process was carried out at a constant voltage of 30 V for 1 min. Then, the coated sample was dried at room temperature for 2 h and employed as an electrode for the subsequent experiments.

To obtain a MMSNs/CNTs composite coating as the second layer, the electrophoretic codeposition (CO-EPD) strategy was carried out using the following procedures: MMSNs were dispersed into an ethanol solution (10 mL) of $Mg(NO_3)_2{\cdot}6H_2O$ (1 mM) and ultrasonicated for 10 min. Then, CNTs were added, and another ultrasonic treatment of 10 min was performed. The homogeneous mixed solution with a black color was used for CO-EPD, and the total mass of MMSNs and CNTs was maintained at 4 mg. A constant voltage of 30 V and deposition time of 2 min were applied during the fabrication process. Finally, the stent was extracted from the suspension and dried at 70 °C in a vacuum oven overnight. The mass ratios of MMSNs/CNTs for the second layer were regulated to 3:1 and 5:1, and the corresponding coated stents were denoted as 316L-BMS@CNTs@M/C-3 and 316L-BMS@CNTs@M/C-5, respectively.

Mechanical Evaluation of the Nanostructured Coatings In Vitro. The mechanical properties of the nanostructured coatings deposited onto 316L-BMS were evaluated by expanding the stents with a balloon system in vitro. A coated stent was rode and crimped onto a shrunken balloon of a catheter, and a pressure of 12 atm was then employed to make the balloon and stent fully expand. The integrities and morphologies of the coatings before and after the

expansion were observed with field-emission scanning electron microscope (FE-SEM).

Hemolysis Test of Different Stent Samples. The hemolysis experiments were carried out according to a previous report.[46] That is, 4 mL of heparinized whole blood was first diluted by adding 5 mL of normal saline. 316L-BMS and 316L-BMS@CNTs@M/C-3 were dipped in separate standard tubes containing 10 mL of normal saline and 0.2 mL of the diluted blood. Similarly, positive and negative control samples were prepared by adding 10 mL of water and normal saline, respectively, to 0.2 mL of the diluted blood. Then, all of the samples were incubated at 37 °C for 60 min. Afterward, the stents were removed, and all of the solutions were centrifuged at 3000 rpm for 5 min. The supernatant was transferred to a 96-well plate, and the absorbance was measured at 545 nm by a microplate reader (BioTek, USA). The hemolysis percentages were calculated using the following formula:

$$\text{hemolysis \%} = (\text{Abs of sample} - \text{Abs of negative control}) / (\text{Abs of positive control} - \text{Abs of negative control}) \times 100\%$$

Platelet Adhesion Test. The platelet adhesion test was conducted to evaluate the thrombogenicity of different samples as follows.[46] Heparinized anticoagulated whole blood was first centrifuged at 1500 rpm for 15 min to obtain platelet-rich plasma (PRP). Then, the samples of 316L-BMS and 316L-BMS@CNTs@M/C-3 were sequentially added into PRP solutions and incubated at 37 °C for 1 h. After incubation, all of the samples were gently rinsed with phosphate buffered saline (PBS) three times to remove nonspecifically adherent platelets. Finally, the samples were fixed, dehydrated, freeze-dried, and coated with gold for SEM observation. Five random fields of view under SEM were counted, and values were expressed as the average number of adherent platelets per mm^2 of surface.

Quantification of the RAPA-Loading Capacity. To study the loading amount of RAPA for MMSNs as a control, a modified method was performed according to our previous work.[35] That is, dried nanoparticles (3 mg) were suspended into toluene solution (3 mL) of RAPA (200 $\mu g\ mL^{-1}$) and shaken for 1 h at room temperature. The supernatant was separated by a magnetic field and analyzed by the high-performance liquid chromatography (HPLC) method to determine the amount of RAPA. Similar as that for the coated samples, a stent was immersed into a RAPA-toluene solution (1.5 mL, 200 $\mu g\ mL^{-1}$) for 1 h. Then, the RAPA-loaded stent was extracted from the solution to dry, and the supernatant was detected by HPLC to calculate the drug-loading amount. The stent was dried overnight at room temperature in a vacuum oven.

Pharmacokinetic Study In Vitro. The release profile of the RAPA-eluting stent was evaluated using a previously reported method.[47] Briefly, deployed stents (n = 3) were immersed in 1 mL of PBS (pH 7.4) at 37 °C and shaken at a speed of 100 rpm. At certain time intervals, the release medium was completely removed for HPLC analysis and replaced with the same volume of fresh medium. The results were expressed as the cumulative percentage of RAPA released over time.

Characterization. Transmission electron microscopy (TEM) images of MMSNs and CNTs were recorded on a JEM 2010 (JEOL, Japan) instrument with a 200 kV accelerated voltage. The hydrodynamic diameter distribution and the zeta potential of various samples were performed on a Zetasizer Nano instrument (Malvern, UK) at 298 K. The nitrogen sorption isotherm was measured with a Micromeritcs ASAP2010 analyzer (USA) at 77 K. The specific surface area was calculated by the Brunauer–Emmett–Teller (BET) method[48] in a linear relative pressure range between 0.05 and 0.25. The pore-size distribution was derived from the desorption branch of the isotherm by the NLDFT method[49] using the Quantachrome Autosorb 1 software (Quantachrome Instruments, USA). The concentration of RAPA was measured on a Shimadzu LC-20 AD high-performance liquid chromatography (HPLC) with a SPD-20A UV–vis detector operated at 280 nm (Shimadzu, Japan). The mobile phase was 60% methanol, 16% acetonitrile, and 24% water with a flow rate of 1 mL min^{-1}. The internal standard method was used to determine the concentration of RAPA by comparing the peak area of the sample with that of a standard solution. Scanning electron microscopy (SEM) images were obtained by a Sirion 200 field-emission scanning electron microscope (FE-SEM, FEI, Netherlands). To analyze the elements distribution in the assembled nanostructured coatings qualitatively, the energy dispersive X-ray spectrum was measured with an INCA X-Act energy dispersive X-ray spectroscope (EDS, Oxford, UK).

In Vivo Study of the Rate of Re-endothelialization. Animal experiments were approved by the Animal Care and Use Committee of Shanghai Jiao Tong University. Briefly, 36 male New Zealand white rabbits (SLACCAS, Shanghai, China) with a body weight between 2.5 and 3.0 kg were randomly implanted with 316L-BMS@CNTs@M/C-3 DES (n = 18) and P-FBII DES (n = 18) and were followed for 14, 21, or 28 days. Three days before the procedure and throughout the following period, all animals orally received 10 mg of aspirin and 12.5 mg of clopidogrel daily.

The procedure for stent implantation was performed under digital subtraction angiography (INNOVA2100, GE, USA). Animals were first sedated and anesthetized with intravenous ketamine (20 mg/kg) and atropine (1 mg). The right common iliac arterial access was achieved by a 20G puncture needle (Terumo, Tokyo, Japan), and abdominal arterial angiography was then performed after intra-arterial administration of heparin (100 IU/kg). After advancement of a 0.014 in. runthrough guidewire (Terumo, Tokyo, Japan) into the aorta with the tip near the aortic arch, the stent was deployed in the aorta abdominalis 5–10 mm below the origin of bilateral renal arteries. The balloon was inflated to 12 atm for a period of 30 s with the stent vessel ratio of 1.1:1. The arteriotomy and dermal layers were sutured after the catheter, wire, and sheath were removed.

The stented arterial segments, obtained at 14, 21, and 28 days, were processed for SEM analysis. The stented arterial segments were first flushed with PBS for 1 min followed by a gentle flush with 10% buffered formalin for 30 s. Stented segments were further fixed with 2.5% glutaraldehyde in 0.1 M sodium cacodylate buffer overnight and were then washed three times with cacodylate buffer. Postfixation was completed with 1% osmium tetroxide in 0.1 M cacohylate buffer followed by serial dehydration with ethanol (30, 50, 70, 90, 95, and 100%) and subsequent critical-point drying with CO_2. After drying, samples were gold sputtered and visualized under SEM. Regions of interest were photographed at incremental magnifications. From these SEM images, the percentage of re-endothelialized area of the total stented area was estimated with the Image-Pro Plus system (Roper Industries, California, USA).

Statistical Analysis. Each experiment was carried out in triplicate at least. Data are presented as mean ± standard deviation (SD). Differences between the mean values of two groups were tested by Student's t test. $P < 0.05$ was considered to be statistically significant.

3. RESULTS AND DISCUSSION

3.1. Characterization of MMSNs and CNTs. The as-prepared MMSNs have a uniform and discrete spherical shape with a mean particle diameter of 50 ± 10 nm, as shown in their representative transmission electron microscopy (TEM) images (Figures 2a and S1 in the Supporting Information). Most MMSNs possess a core–shell-composite structure with a single core center located in the mesoporous silica shell layer. Wormhole-like mesopores arranged radially to the surface are found, which is consistent with the results reported previously.[45,50] As for the CNTs used in this study, 1D tubular structures with a typical single wall can be clearly obseved from Figure 2b. The carboxylated CNTs have a length of 389 ± 157 nm (Figure 2e), and their diameter is less than 2 nm. In addition, the hydrodynamic diameter distribution of MMSNs in water has a single peak centered at 80 nm, as shown in Figure 2c. The nitrogen isotherm measurement for MMSNs exhibits a

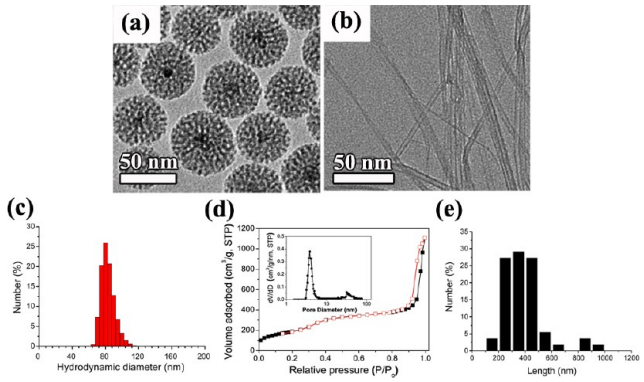

Figure 2. Representative TEM images of (a) MMSNs and (b) CNTs. (c) Hydrodynamic diameter distribution of MMSNs in water. (d) Nitrogen sorption isotherm at 77 K for MMSNs (the inset shows the corresponding pore-size distribution). (e) Length distribution of CNTs measured from TEM images.

type IV isotherm with the H1 hysteresis loop (Figure 2d). The obvious nitrogen-condensation step at the relative pressure P/P_0 = 0.25−0.4 is reflected in a narrow pore-size distribution curve (Figure 2d, inset) with a sharp peak centered at 3.8 nm, which supports the observed pore structures (Figure 2a). The surface area and pore volume of MMSNs are determined to be 696 m^2/g and 0.44 cm^3/g, respectively, indicating their high potential in loading a sufficient amount of drug or other biomolecules.

3.2. Fabrication of Different Nanostructured Coatings on Stents. Because MMSNs have proven to be excellent vehicles for loading RAPA,[34−36] a widely used drug for DES in the clinic, it is worth trying to assemble these nanoparticles onto stents as a drug-storage coating. Considering the probable brittleness of the individual MMSNs assembled coatings, we designed a novel two-layered CNTs@MMSNs/CNTs composite coating. That is, a thin CNTs film is first deposited onto stents as the buffer layer and then a second MMSNs/CNTs coating is fabricated as the functional layer, as shown in Figure 1. The corresponding coated samples are denoted as 316L-BMS@CNTs@M/C-X (X represents the added mass ratios of MMSNs/CNTs for the second layer).

The scanning electron microscopy (SEM) images of these coating samples are shown in Figure 3. For 316L-BMS@CNTs@M/C-3, there is no doubt that a uniform coating is successfully constructed on the complex-structured stent with no cracking and debonding (Figure 3a,b). Moreover, it seems

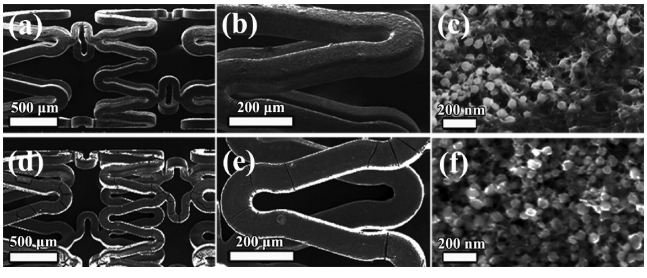

Figure 3. SEM images of different two-layered CNTs@MMSNs/CNTs composite coatings on stents. (a−c) 316L-BMS@CNTs@M/C-3 and (d−f) 316L-BMS@CNTs@M/C-5. For 316L-BMS@CNTs@M/C-X, X represents the added mass ratios of MMSNs/CNTs for the second layer.

that the spherical nanoparticles infiltrate into the porous CNTs layer homogeneously, building a composite coating with unique network nanostructures (Figure 3c). The thickness and structure of this two-layered coating can also be clearly observed from the SEM image (Figure S2 in the Supporting Information). The cross section shows that the total thickness of this two-layered coating is estimated to be ∼8.6 μm, wherein the CNTs layer is ∼0.8 μm and the MMSNs/CNTs layer is ∼7.8 μm. As the ratio of MMSNs/CNTs increases to 5, several cracks begin to develop in the second layer (Figure 3d,e), indicating that the coating contracted a lot for the samples with more incorporated MMSNs during the drying process with the evaporation of ethanol.[51] This result is supported by its nanotopology (Figure 3f). The CNTs are difficult to distinguish for their twining around the nanoparticles; thus, the accumulation of MMSNs lead to large tensile stresses among this coating. In summary, this "two-layered" strategy has successfully constructed a crack-free composite coating with a high MMSNs/CNTs ratio (determined to be 3 for the second layer) simultaneously, which will provide a potential platform for carrying RAPA.

To investigate the role of the inner CNTs layer, the single MMSNs/CNTs coatings were directly deposited onto stents (see the experimental methods in the Supporting Information), denoted as 316L-BMS@M/C-X (X represented the ratios of MMSNs/CNTs). SEM characterization of these MMSNs/CNTs composite coatings is shown in Figure 4. For 316L-

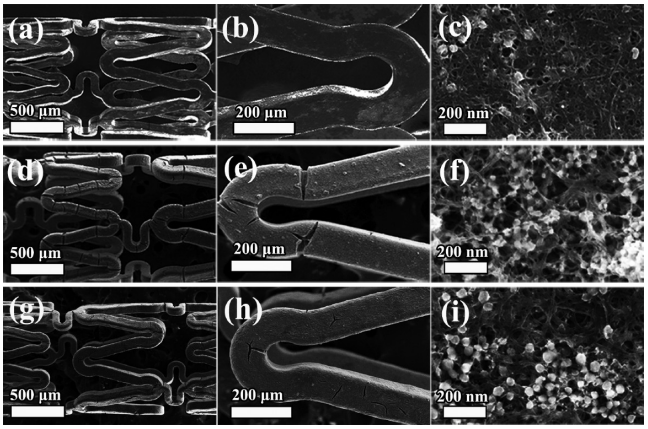

Figure 4. SEM images of different MMSNs/CNTs composite coatings on stents. (a−c) 316L-BMS@M/C-1, (d−f) 316L-BMS@M/C-2, and (g−i) 316L-BMS@M/C-3. For 316-BMS@M/C-X, X represents the added mass ratios of MMSNs/CNTs.

BMS@M/C-1, a crack-free film is obtained because of the high ratio of CNTs (Figure 4a,b). Unfortunately, the cracks of an "interrupted" or "incompletely developed" type appear in the coatings when the ratio of MMSNs/CNTs is not less than 2 (Figure 4e,h). Of note and differing from our expectation, more cracks exist in 316L-BMS@M/C-2 when compared with 316L-BMS@M/C-3, which is perhaps ascribed to the increased number of aggregates of MMSNs (Figure 4e,f). Moreover, these MMSNs/CNTs composite coatings also have the network nanostructures (Figure 4c,f,i), which is similar to 316L-BMS@CNTs@M/C-3.

Because the ratio of MMSNs/CNTs used for 316L-BMS@M/C-3 is the same as that used for the second layer of 316L-BMS@CNTs@M/C-3, the occurring cracks are definitely ascribed to the absence of the inner CNTs layer. From the

above results, it is confirmed that the CNTs film acts as a buffer layer to inhibit the formation of cracks, and the tensile stresses engendered by the contraction of the second composite coating are fully released to the CNTs layer. Although a crack-free film could also be obtained using the single-layer strategy, when taking the practical application into consideration, the mass ratio of MMSNs/CNTs should not be more than 1, which will certainly lower the potential RAPA-loading amount.

Furthermore, we also prepared the individual MMSNs or CNTs coatings as a control (described in the experimental methods in the Supporting Information), and the samples are named 316L-BMS@MMSNs and 316L-BMS@CNTs, respectively. There is no debonding and shedding occurring for the MMSNs coating, and the nanoparticles are packed closely with an ordered arrangement (Figure S3a,b in the Supporting Information). However, it is disappointing to find numerous cross-linked cracks of ~5−15 μm in width, which is much different from the interrupted or incompletely developed ones in the MMSNs/CNTs composite coatings. For 316L-BMS@CNTs, it is certain that a rather uniform and smooth coating without cracking is obtained (Figure S3c in the Supporting Information), showing an excellent mechanical property because of the composition of the CNTs. The eletrophoretically deposited CNTs lie in random orientations and interwine with each other, forming an impressive porous network on the stent (Figure S3d in the Supporting Information).

Although CNTs are inorganic materials and their assembled coating tends to contract during the drying process, the flexibility of CNTs and the strong van der Waals interactions suppress the development of tensile stresses;[52−54] thus, no formation and propagation of cracks is found in the CNTs coating. Indeed, it is the incorporation of CNTs that constructed the netted layer and separated MMSNs from each other, thus reducing the capillary pressure and inhibiting the propagation of cracks in the samples of 316L-BMS@M/C-X and 316L-BMS@CNTs@M/C-X. It is believed that the energies produced by the formation of cracks are sufficiently released via CNTs.

3.3. Mechanism of Assembling the MMSNs/CNTs Composite Coatings. To investigate the electrophoretic codeposition (CO-EPD) mechanism of MMSNs and CNTs, zeta potential (ZP) measurements were conducted in an ethanol solution with or without Mg^{2+}. As shown in Figure 5a, the MMSNs have a negative charge (−21.53 ± 1.90 mV) in ethanol because of the dissociation of Si−OH, whereas a positive ZP value (+11.45 ± 0.95 mV) is exhibited in the ethanol solution containing 1 mM Mg^{2+}, which is ascribed to the electrostatic adsorption between MMSNs and Mg^{2+}. The charge reversal occurs for the carboxylated CNTs as well, in which the nanotubes possess a negative ZP value (−35.20 ± 2.75 mV) in ethanol for their modification with −COOH, whereas a positive charge (+27.28 ± 1.03 mV) is obtained after the addition of Mg^{2+}. Actually, both MMSNs and CNTs were observed to move toward and deposit onto the cathode (stent) during the preparation of 316L-BMS@MMSNs and 316L-BMS@CNTs.

As for the CO-EPD process of MMSNs and CNTs in our system, a possible mechanism is proposed as depicted in Figure 6. First, MMSNs were dispersed into the 1 mM Mg^{2+}-containing ethanol solution to form positively charged nanoparticles (denoted MMSNs@Mg^{2+}). Then, the negatively charged CNTs were added into the suspension, and they assemble with MMSNs@Mg^{2+} via electrostatic interactions.

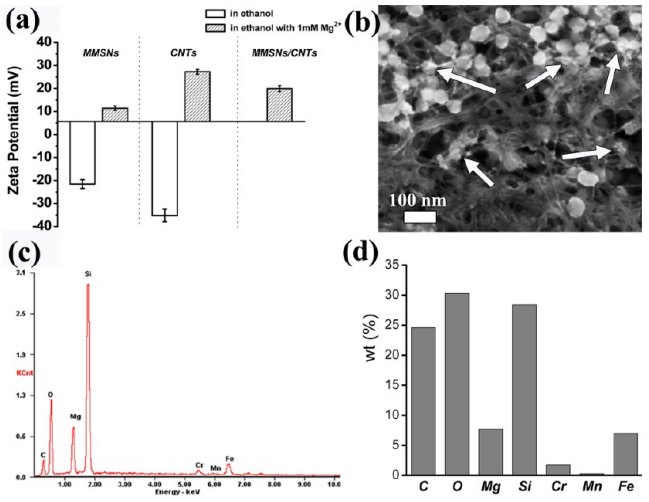

Figure 5. (a) Zeta potential values of different nanomaterials in an ethanol solution with or without 1 mM Mg^{2+}. (b) High-magnification SEM image of 316L-BMS@CNTs@M/C-3 showing the interactions between MMSNs and CNTs. The MgO nanocrystals are marked with white arrows. (c) EDS spectrum and (d) the corresponding histogram showing the elements distribution in the MMSNs/CNTs composite coating for sample 316L-BMS@CNTs@M/C-3.

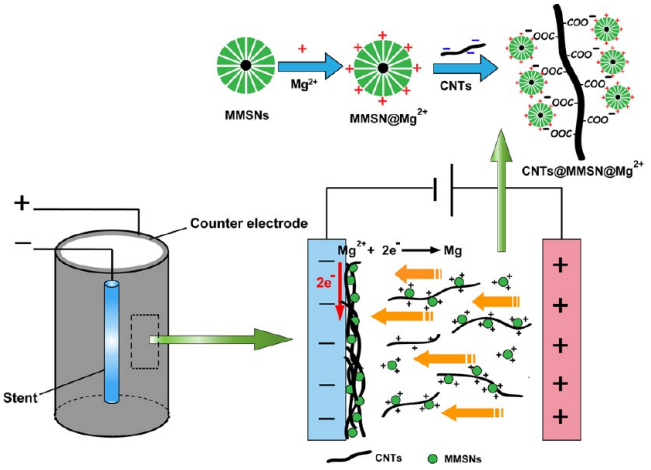

Figure 6. Illustration of the proposed mechanism for the CO-EPD process of MMSNs and CNTs.

Because MMSNs@Mg^{2+} can be regarded as a positively charge centralized carrier, they will be adsorbed around CNTs more preferentially than the individual Mg^{2+} and thus a complex CNTs@MMSNs@Mg^{2+} is formed as described in Figure 6. Theoretically, the negatively charged surface of the CNTs will be shielded by MMSNs@Mg^{2+} to obtain a positive surface. To confirm our hypothesis, we measured the ZP value of the EPD bath for 316L-BMS@M/C-3, and a positive value (+19.93 ± 1.35 mV) was obtained (Figure 5a). In fact, there should exist three possible forms in the solution, MMSNs@Mg^{2+}, CNTs@Mg^{2+}, and CNTs@MMSNs@Mg^{2+}. Under the electric field, all three forms move toward the cathode (stent), and we assume that the Mg^{2+} ions would be probably reduced to form metallic Mg when they arrive at the substrate. Then, the metallic Mg would be further oxidized to MgO in air during the drying process. Because of the high electrical conductivities of CNTs, electrons are conducted from the stent to the outer layer of the

coating,[55] allowing the codeposition of MMSNs and CNTs to proceed successfully.

The high-magnification SEM image shows the interations between MMSNs and CNTs in the constructed composite coating of 316L-BMS@CNTs@M/C-3 (Figure 5b). It seems that some ~2−5 nm sized nanocrystals with irregular morphologies appear in this coating (marked with white arrows), especially in the interfaces of MMSNs and CNTs, indicating that the added Mg^{2+} ions act as bridges in the CO-EPD process. The energy dispersive X-ray spectrum (EDS) illustrates that the Mg element is incorporated into the coating with a mass fraction of 7.74% (Figure 5c,d), verifying the presence of MgO in 316L-BMS@CNTs@M/C-3. For the prepared MMSNs or CNTs coatings, MgO is proved to exist as well (Figure S4 in the Supporting Information). The addition of Mg^{2+} reduces the reduction potential of the EPD process and makes the deposition occur more easily. It has been proved that the formed MgO from Mg^{2+} at the surface of the cathode will act as a binder, resulting in the improved adhesion of the assembled films to the substrate.[56,57] Because both MMSNs and CNTs have a negative zeta potential in ethanol, they can codeposit onto the anode during the EPD process without adding Mg^{2+}. However, this strategy will make the stent become oxidized under the electric field, leading to the release of metal ions to the coatings, which limits its practical application. As a control, blank experiments were carried out for constructing a MMSNs coating in the absence of Mg^{2+}, and an inhomogeneous and easily peeled off film was obtained, showing poor adhesion to the stent (Figure S5 in the Supporting Information). That is to say, the addition of Mg^{2+} is rather important for our system.

3.4. In Vitro Evaluation of Different Nanostructured Coatings. Cardiovascular stents should be able to endure a strict expansion process in the clinic. However, the polymer coatings are well suited for the deformation of the metallic stents because of their excellent flexibilities, which is a big challenge for inorganic coatings. The integrity and morphology of different nanostructured coatings after expansion are shown in their typical SEM images (Figure 7a). For 316L-BMS@MMSNs, a serious shedding is observed because of the brittleness of this coating, resulting in a partial exposure of the metal surface (Figure 7a1,a2). As with the incorporation of CNTs, the mechanical properties of 316L-BMS@M/C-3 have been improved to some extent (Figure 7a3,a4). That is, this composite coating shows an obvious peeling away from the strengthening rings, resulting from the propagation of cracks during expansion (Figure 7a3); however, only minor shedding and defects are exhibited on strut sections (Figure 7a4). The micrometer-sized debris shedding from the two coatings mentioned above have high risks for increasing vascular inflammatory.[26] To promote the biosafety of this polymer-free strategy as much as possible, we designed a two-layered coating of 316L-BMS@CNTs@M/C-3 with a thin CNTs film as a buffer layer, which has the most outstanding flexibilities, as shown in Figure 7a5,a6. It is observed clearly that only seldom nanometer-sized shedding or defects occurr on the strengthening rings without cracking (Figure 7a5), and no damage is found on strut sections (Figure 7a6), indicating that the inner CNTs layer could adapt to the expanded stents appropriately. The two-layered composite coating covered and adhered to the stent well after expansion process, showing a high potential for practical application.

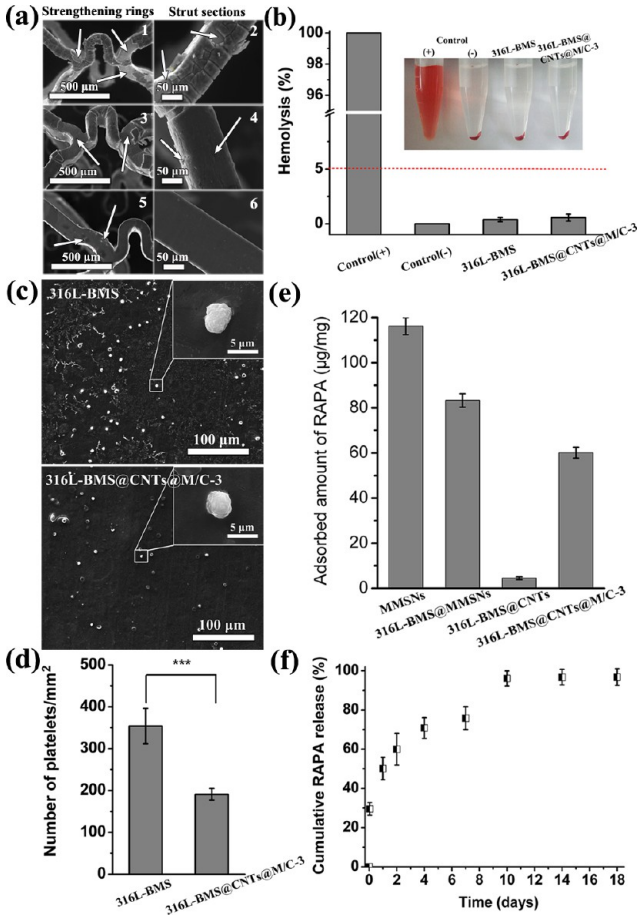

Figure 7. (a) SEM images of different coating samples after balloon expansion under a pressure of 12 atm: (1, 2) 316L-BMS@MMSNs, (3, 4) 316L-BMS@M/C-3, and (5, 6) 316L-BMS@CNTs@M/C-3. The shedding sections or defects are marked with white arrows. (b) Hemolysis results of different samples in contact with blood. The released hemoglobin from the damaged red blood cells (RBCs) in the supernatant can be seen from the inset photograph. (c) SEM images of adherent platelets on the surfaces of the samples: 316L-BMS and 316L-BMS@CNTs@M/C-3 incubated in PRP for 1 h. The inset shows the representative morphology of a platelet. (d) Bar graph showing the numbers of adherent platelets on the surfaces of different samples, as calculated from their corresponding SEM images. Significant differences between two groups are indicated (n = 5, ***P < 0.001). (e) Histogram showing the RAPA-loading capabilities of MMSNs and different coating sampels. (f) In vitro release profile of RAPA from 316L-BMS@CNTs@M/C-3 DES platform in PBS (pH 7.4) at 37 °C.

Because stents are in contact with blood directly after implantation, the in vitro hemolysis assay and platelet-adhesion test were performed to evaluate their hemocompatibility. The hemolysis percentage represents the destructive degree of the implant materials to erythrocytes, and the value of 316L-BMS@CNTs@M/C-3 (0.56 ± 0.32%) is slightly higher than that of 316L-BMS (0.38 ± 0.19%), as shown in Figure 7b. However, the values of both groups are much lower than 5%, which is a judging criterion for excellent blood compatibility in clinical applications.[58] Figure 7c shows the morphologies of the platelets adhering to the surfaces of the samples. It is obvious that more platelets are detected on the surfaces of 316L-BMS than of 316L-BMS@CNTs@M/C-3. Moreover, almost all platelets on both samples kept a nearly round shape without

any pseudopodia-like structures, implying negative activation.[46] The numbers of adherent platelets on the surfaces of different samples are given in Figure 7d. The value of 316L-BMS@CNTs@M/C-3 is determined to be 191 ± 14 mm^{-2}, which is significantly lower than 354 ± 42 mm^{-2} for 316L-BMS (***P < 0.001). The results illustrate that the coated stents have a lower potential for thrombosis, thus owning a better hemocompatibility than 316L-BMS.

RAPA is a drug molecule with three hydroxyl groups (see Figure S6 in the Supporting Information) that could form hydrogen bonds with the numerous Si−OH on the inner/outer surfaces of MMSNs.[36] The RAPA-loading capabilities of MMSNs and different coating samples were evaluated (Figure 7e). The adsorbed amount is 116.27 ± 3.84 and 83.27 ± 2.96 μg/mg for MMSNs and their assembled coating, respectively. The decreased values should be mainly attributed to the incorporation of MgO, which reduces the mass ratio of MMSNs in the coating. Considering the high loaded RAPA amount for 316L-BMS@MMSNs, we think that the formation of MgO did not block the mesopores of MMSNs, and the TEM image confirms the maintained mesoporous structures of the nanoparticles peeled off of this coating (Figure S7 in the Supporting Information). For 316L-BMS@CNTs, a minor value of 4.47 ± 0.65 μg/mg is obtained, indicating that CNTs only act as reinforcing elements in the constructed coatings, contributing little to the adsorption of RAPA. The loading amount further decreases to 60.10 ± 2.43 μg/mg for the two-layered coating sample of 316L-BMS@CNTs@M/C-3, owing to the incorporation of CNTs. The detailed information for coating samples is supplied as well (Table S1 in the Supporting Information). The loaded RAPA amout is calculated to be 52.87 ± 1.31 μg on a stent of 316L-BMS@CNTs@M/C-3, which ensures its adequate drug-loading capacities and is very similar to the reported HAp-coated microporous stent platform.[28]

The in vitro RAPA release from the 316L-BMS@CNTs@M/C-3 DES platform shows that the petcentage of cumulative drug release is 29.5% at 1 h and 50.1% at 24 h (Figure 7f), which is minimally different from the polymer-coated RAPA-eluting stent platform reported by our co-workers recently.[47] The initial burst release, which could be of benefit for quickly reaching the effective treatment concentration, is due to the adsorption of drugs in the external pores of MMSNs.[59] In the following stage, a prolonged release profile is observed with a cumulative petcentage of 59.9% at 2 days, 75.8% at 7 days, and 96.8% at 14 days. The subsequent slow release is ascribed to the inner RAPA molecules residing in the mesopores.

3.5. In Vivo Study of the Rate of Re-endothelialization. To evaluate the rate of re-endotheliazation in vivo for the nanostructured 316L-BMS@CNTs@M/C-3 DES, these stents (n = 18) were implanted in the abdominal aorta of New Zealand white rabbits as described in the Experimental Section (the schematic illustration is shown in Figure 8a), and the commercial polymer-coated RAPA-eluting Firebird-II stents (P-FBII DES, n = 18) were employed as a control group. SEM images of vessel walls in the two groups at 14, 21, and 28 days post stent implantation are shown (Figure 8b). It is evident that the P-FBII DES have considerable uncovered areas by endothelial cells (their existence is proved by Figure S8 in the Supporting Information) in comparison with the 316L-BMS@CNTs@M/C-3 DES before 21 days, and even an early inflammatory reaction is observed at 14 days (Figure 8b), which should be the result of the existing polymer coatings. However,

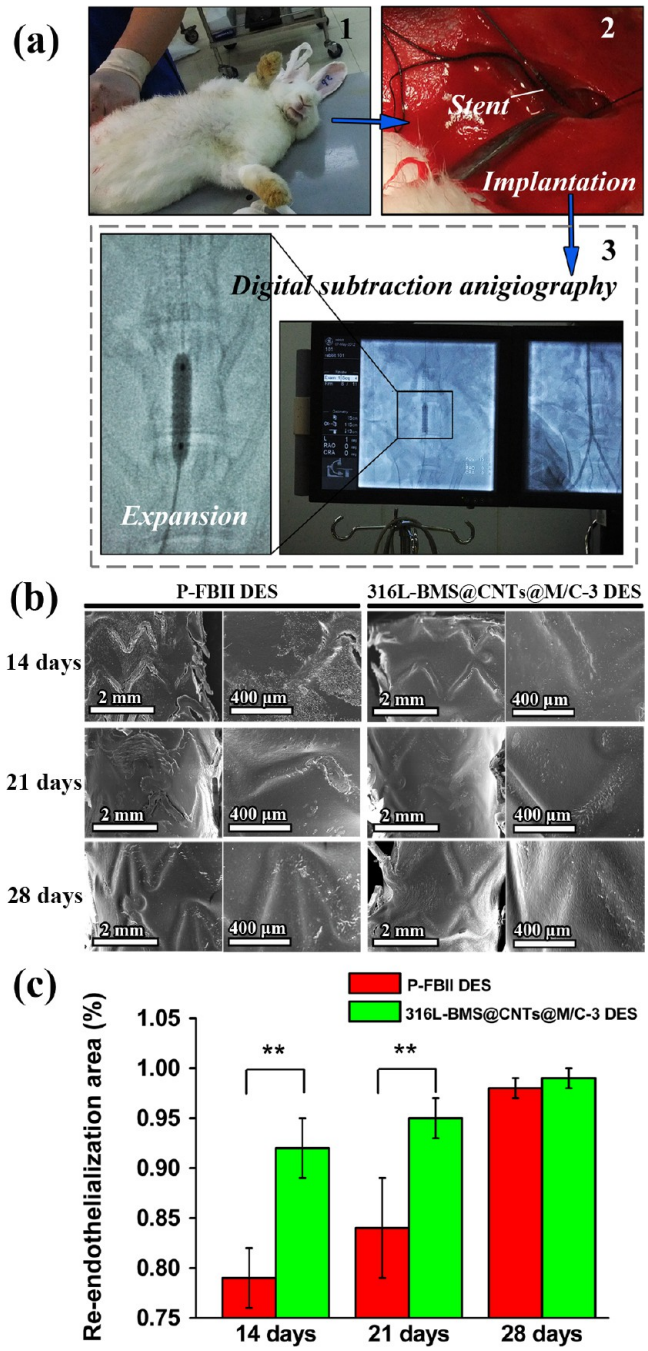

Figure 8. (a) Schematic illustration of the surgical procedure for stent implantation. (b) SEM images of vessel walls in the P-FBII DES and 316L-BMS@CNTs@M/C-3 DES groups at 14, 21, and 28 days post stent implantation. (c) Bar graph showing the percentage of re-endotheliazation area for the different DES groups, as calculated from their corresponding SEM images. Significant differences between two groups are indicated (n = 6, **P < 0.01).

these disparities between the two groups almost disappear completely at 28 days. Figure 8c displays the percentage of re-endotheliazation area for the different DES samples, as calculated from their corresponding SEM images. The values are determined to be 92 ± 3% and 95 ± 2% for 316L-BMS@CNTs@M/C-3 DES at 14 and 21 days, respectively, which are significantly higher than 79 ± 3% and 84 ± 5% for P-FBII DES (**P < 0.01). At 28 days, an endothelial cell coverage of 99 ±

1% and 98 ± 1% are obtained, indicating no discrepancy between these two groups.

From the impressive results mentioned above, it is confirmed that the 316L-BMS@CNTs@M/C-3 DES has the obvious advantage of rapid re-endotheliazation in the early stage when compared with P-FBII DES. We attribute this phenomenon to the following reasons. (i) The polymer-free component has improved the biocompatibility of the drug-eluting coating by reducing the probability of the inflammatory reactions that always accompany polymer coatings.[11,14,17] (ii) The unique 3D nanostructured surfaces of 316L-BMS@CNTs@M/C-3 DES have positive effects on cell attachment and proliferation in comparison with conventional (microstructured) surfaces, which has been proved by available reports previously;[41−43] thus, an accelerated endothelialization is observed. Actually, the rapid re-endotheliazation ability of the 316L-BMS@CNTs@M/C-3 DES is probably of great importance to reduce the risks of LST, which must be further studied in the future.

4. CONCLUSIONS

We adopted the EPD method to explore the possibility of constructing uniform MMSNs/CNTs composite coatings on cardiovascular stents. A crack-free two-layered coating with impressive network nanotopology is obtained by regulating the composition and structures. That is, a thin CNTs film acts as an inner buffer layer, and a second MMSNs/CNTs composite coating acts as a functional layer. We propose a possible mechanism of the CO-EPD process of MMSNs and CNTs in which the addition of Mg^{2+} plays an important role. Moreover, the excellent mechanical flexibility and blood compatibility of this polymer-free coating are exhibited in vitro, the RAPA-loading capability of 316L-BMS@CNTs@M/C-3 is determined to be 60.10 ± 2.43 μg/mg, and the drugs could be continuously released to 2 weeks. Finally, an in vivo study shows that this nanostructured DES has the obvious advantage of rapid re-endotheliazation in the early stage when compared with the commercial P-FBII DES, which is probably of great importance to reduce the risk of LST. There is no doubt that this study will provide new ideas and reliable data to design novel functional coatings that could accelerate the re-endothelialization process and improve the in vivo biosafety of DES. However, further long-term evaluation is needed to confirm their validity in vivo.

■ ASSOCIATED CONTENT

Ⓢ Supporting Information

Additional experimental details; TEM image of the as-synthesized MMSNs in a low magnification; SEM image of 316L-BMS@CNTs@M/C-3 showing the transverse structures; SEM images of stent samples coated with different nanomaterials; EDS spectrums showing the elements distribution in the assembled coatings for 316L-BMS@MMSNs and 316L-BMS@CNTs; SEM images of 316L-BMS@MMSNs in the absence of Mg^{2+} showing poor adhesion of the coating to the stent; molecular structure of RAPA; TEM image of MMSNs peeled off of the 316L-BMS@MMSNs; weight and loaded drug amount for different samples; and high-magnification SEM images of vessel walls in the P-FBII DES and 316L-BMS@CNTs@M/C-3 DES groups at 14 days post stent implantation. This material is available free of charge via the Internet at http://pubs.acs.org.

■ AUTHOR INFORMATION

Corresponding Authors

*E-mail: zhangruiyan@263.net (R.Z.); Tel: +86-21-64370045.
*E-mail: hcgu@sjtu.edu.cn (H.G.); Tel: +86-21-62932149.

Author Contributions

[§]These authors contributed equally to this work. The manuscript was written through contributions of all authors. All authors have given approval to the final version of the manuscript.

Notes

The authors declare no competing financial interest.

■ ACKNOWLEDGMENTS

This work was supported by an ERC grant (11DZ2211000) from the Science and Technology Commission of Shanghai and by SJTU funding (AE4160003). The authors thank the Instrumental Analysis Center of Shanghai Jiao Tong University and the Nanotechnology and Application National Engineering Research Centre for the characterization of materials. Special thanks to Dr. Liqin Xiong for word processing assitance.

■ REFERENCES

(1) Sigwart, U.; Puel, J.; Mirkovitch, V.; Joffre, F.; Kappenberger, L. *N. Engl. J. Med.* **1987**, *316*, 701−706.
(2) Erbel, R.; Haude, M.; Höpp, H. W.; Franzen, D.; Rupprecht, H. J.; Heublein, B.; Fischer, K.; Jaegere, P.; Serruys, P.; Rutsch, W.; Probst, P. *N. Engl. J. Med.* **1998**, *339*, 1672−1678.
(3) Ma, X.; Wu, T.; Robich, M. P. *Intervent. Cardiol.* **2012**, *4*, 73−83.
(4) Hoffmann, R.; Mintz, G. S.; Dussaillant, G. R.; Popma, J. J.; Pichard, A. D.; Satler, L. F.; Kent, K. M.; Griffin, J.; Leon, M. B. *Circulation* **1996**, *94*, 1247−1254.
(5) Farb, A.; Sangiorgi, G.; Carter, A. J.; Walley, V. M.; Edwards, W. D.; Schwartz, R. S.; Virmani, R. *Circulation* **1999**, *99*, 44−52.
(6) Fattori, R.; Piva, T. *Lancet* **2003**, *361*, 247−249.
(7) Ranade, S. V.; Miller, K. M.; Richard, R. E.; Chan, A. K.; Allen, M. J.; Helmus, M. N. *J. Biomed. Mater. Res.* **2004**, *71A*, 625−634.
(8) Wessely, R. *Nat. Rev. Cardiol.* **2010**, *7*, 194−203.
(9) Moses, J. W.; Leon, M. B.; Popma, J. J.; Fitzgerald, P. J.; Holmes, D. R.; O'Shaughnessy, C.; Caputo, R. P.; Kereiakes, D. J.; Williams, D. O.; Teirstein, P. S.; Jaeger, J. L.; Kuntz, R. E. *N. Engl. J. Med.* **2003**, *349*, 1315−1323.
(10) Joner, M.; Finn, A. V.; Farb, A.; Mont, E. K.; Kolodgie, F. D.; Ladich, E.; Kutys, R.; Skorija, K.; Gold, H. K.; Virmani, R. *J. Am. Coll. Cardiol.* **2006**, *48*, 193−202.
(11) Lüscher, T. F.; Steffel, J.; Eberli, F. R.; Joner, M.; Nakazawa, G.; Tanner, F. C.; Virmani, R. *Circulation* **2007**, *115*, 1051−1058.
(12) Stone, G. W.; Moses, J. W.; Ellis, S. G.; Schofer, J.; Dawkins, K. D.; Morice, M. C.; Colombo, A.; Schampaert, E.; Grube, E.; Kirtane, A. J.; Cutlip, D. E.; Fahy, M.; Pocock, S. J.; Mehran, R.; Leon, M. B. *N. Engl. J. Med.* **2007**, *356*, 998−1008.
(13) Daemen, J.; Wenaweser, P.; Tsuchida, K.; Abrecht, L.; Vaina, S.; Morger, C.; Kukreja, N.; Jüni, P.; Sianos, G.; Hellige, G.; Domburg, R. T.; Hess, O. M.; Boersma, E.; Meier, B.; Windecker, S.; Serruys, P. W. *Lancet* **2007**, *369*, 667−678.
(14) Virmani, R.; Guagliumi, G.; Farb, A.; Musumeci, G.; Grieco, N.; Motta, T.; Mihalcsik, L.; Tespili, M.; Valsecchi, O.; Kolodgie, F. D. *Circulation* **2004**, *109*, 701−705.
(15) Finn, A. V.; Nakazawa, G.; Joner, M.; Kolodgie, F. D.; Mont, E. K.; Gold, H. K.; Virmani, R. *Arterioscler., Thromb., Vasc. Biol.* **2007**, *27*, 1500−1510.
(16) Okner, R.; Shaulov, Y.; Tal, N.; Favaro, G.; Domb, A. J.; Mandler, D. *ACS Appl. Mater. Interfaces* **2009**, *1*, 758−767.
(17) Van Der Giessen, W. J.; Lincoff, A. M.; Schwartz, R. S.; Beusekom, M. M.; Serruys, P. W.; Holmes, D. R.; Ellis, S. G.; Topol, E. J. *Circulation* **1996**, *94*, 1690−1697.
(18) O'Brien, B.; Carroll, W. *Acta Biomater.* **2009**, *5*, 945−958.

(19) Ge, J.; Qian, J.; Wang, X.; Wang, Q.; Yan, W.; Yan, Y.; Fan, B.; Ge, L.; Liu, X. *Catheter. Cardiovasc. Interventions* **2007**, *69*, 198−202.
(20) Lee, C.; Lim, J.; Low, A.; Zhang, X.; Kyaing, T.; Chan, M. Y.; Wong, H.; Lim, Y.; Tan, H. *J. Invasive Cardiol.* **2007**, *19*, 182−185.
(21) Vranckx, P.; Serruys, P.; Gambhir, S.; Sousa, E.; Abizaid, A.; Lemos, P.; Ribeiro, E.; Dani, S.; Dalal, J.; Mehan, V.; Dhar, A.; Dutta, A. L.; Reddy, K. N.; Chand, R.; Ray, A.; Symons, J. *EuroIntervention* **2006**, *2*, 310−317.
(22) Wessely, R.; Hausleiter, J.; Michaelis, C.; Jaschke, B.; Vogeser, M.; Milz, S.; Behnisch, B.; Schratzenstaller, T.; Renke-Gluszko, M.; Stöver, M.; Wintermantel, E.; Kastrati, A.; Schömig, A. *Arterioscler., Thromb., Vasc. Biol.* **2005**, *25*, 748−753.
(23) Hausleiter, J.; Kastrati, A.; Wessely, R.; Dibra, A.; Mehilli, J.; Schratzenstaller, T.; Graf, I.; Renke-Gluszko, M.; Behnisch, B.; Dirschinger, J.; Wintermantel, E.; Schömig, A. *Eur. Heart J.* **2005**, *26*, 1475−1481.
(24) Karoussos, I. A.; Wieneke, H.; Sawitowski, T.; Wnendt, S.; Fischer, A.; Dirsch, O.; Dahmen, U.; Erbel, R. *Materwiss. Werksttech.* **2002**, *33*, 738−746.
(25) Wieneke, H.; Dirsch, O.; Sawitowski, T.; Gu, Y. L.; Brauer, H.; Dahmen, U.; Fischer, A.; Wnendt, S.; Erbel, R. *Catheter. Cardiovasc. Interventions* **2003**, *60*, 399−407.
(26) Kollum, M.; Farb, A.; Schreiber, R.; Terfera, K.; Arab, A.; Geist, A.; Haberstroh, J.; Wnendt, S.; Virmani, R.; Hehrlein, C. *Catheter. Cardiovasc. Interventions* **2005**, *64*, 85−90.
(27) Alviar, C. L.; Tellez, A.; Wang, M.; Potts, P.; Smith, D.; Tsui, M.; Budzynski, W.; Raizner, A. E.; Kleiman, N. S.; Lev, E. I.; Granada, J. F.; Kaluza, G. L. *J. Thromb. Thrombolysis* **2012**, *34*, 91−98.
(28) Costa, J. R.; Abizaid, A.; Costa, R.; Feres, F.; Tanajura, L. F.; Maldonado, G.; Staico, R.; Siqueira, D.; Sousa, M. R.; Bonan, R.; Sousa, J. E. *JACC: Cardiovasc. Interventions* **2009**, *2*, 422−427.
(29) Martinez, A. W.; Chaikof, E. L. *Wiley Interdiscip. Rev.: Nanomed. Nanobiotechnol.* **2011**, *3*, 256−268.
(30) Vivero-Escoto, J. L.; Slowing, I. I.; Trewyn, B. G.; Lin, V. S. Y. *Small* **2010**, *6*, 1952−1967.
(31) Popat, A.; Hartono, S. B.; Stahr, F.; Liu, J.; Qiao, S. Z.; Lu, G. Q. *Nanoscale* **2011**, *3*, 2801−2818.
(32) Zhang, L.; Qiao, S.; Jin, Y.; Yang, H.; Budihartono, S.; Stahr, F.; Yan, Z.; Wang, X.; Hao, Z.; Lu, G. Q. *Adv. Funct. Mater.* **2008**, *18*, 3203−3212.
(33) Lu, J.; Liong, M.; Li, Z.; Zink, J. I.; Tamanoi, F. *Small* **2010**, *6*, 1794−1805.
(34) Rosenholm, J. M.; Zhang, J.; Sun, W.; Gu, H. *Microporous Mesoporous Mater.* **2011**, *145*, 14−20.
(35) Zhang, J.; Sun, W.; Bergman, L.; Rosenholm, J. M.; Lindén, M.; Wu, G.; Xu, H.; Gu, H. *Mater. Lett.* **2012**, *67*, 379−382.
(36) Liu, Q.; Zhang, J.; Sun, W.; Xie, Q. R.; Xia, W.; Gu, H. *Int. J. Nanomed.* **2012**, *7*, 999−1013.
(37) Zhang, L.; Geng, W. C.; Qiao, S. Z.; Zheng, H. J.; Lu, G. Q.; Yan, Z. F. *ACS Appl. Mater. Interfaces* **2010**, *2*, 2767−2772.
(38) Harrison, B. S.; Atala, A. *Biomaterials* **2007**, *28*, 344−353.
(39) Ku, S. H.; Lee, M.; Park, C. B. *Adv. Healthcare Mater.* **2013**, *2*, 244−260.
(40) Boccaccini, A. R.; Chicatun, F.; Cho, J.; Bretcanu, O.; Roether, J. A.; Novak, S.; Chen, Q. *Adv. Funct. Mater.* **2007**, *17*, 2815−2822.
(41) Choudhary, S.; Berhe, M.; Haberstroh, K. M.; Webster, T. J. *Int. J. Nanomed.* **2006**, *1*, 41−49.
(42) Fine, E.; Zhang, L.; Fenniri, H.; Webster, T. J. *Int. J. Nanomed.* **2009**, *4*, 91−97.
(43) Brammer, K. S.; Oh, S.; Gallagher, J. O.; Jin, S. *Nano Lett.* **2008**, *8*, 786−793.
(44) Besra, L.; Liu, M. *Prog. Mater. Sci.* **2007**, *52*, 1−61.
(45) Zhang, J.; Li, X.; Rosenholm, J. M.; Gu, H. *J. Colloid Interface Sci.* **2011**, *361*, 16−24.
(46) Zhou, W. R.; Zheng, Y. F.; Leeflang, M. A.; Zhou, J. *Acta Biomater.* **2013**, *9*, 8488−8498.
(47) Zhu, J.; Xiong, X.; Du, R.; Jing, Y.; Ying, Y.; Fan, X.; Zhu, T.; Zhang, R. *Biomaterials* **2012**, *33*, 8204−8212.
(48) Brunauer, S.; Emmett, P. H.; Teller, E. *J. Am. Chem. Soc.* **1938**, *60*, 309−319.
(49) Ravikovitch, P.; Wei, D.; Chueh, W.; Haller, G.; Neimark, A. *J. Phys. Chem. B* **1997**, *101*, 3671−3679.
(50) Kim, J.; Kim, H. S.; Lee, N.; Kim, T.; Kim, H.; Yu, T.; Song, I. C.; Moon, W. K.; Hyeon, T. *Angew. Chem., Int. Ed.* **2008**, *47*, 8438−8441.
(51) Ogihara, H.; Katayama, T.; Saji, T. *J. Colloid Interface Sci.* **2011**, *362*, 560−566.
(52) Rigueur, J. L.; Hasan, S. A.; Mahajan, S. V.; Dickerson, J. H. *Carbon* **2010**, *48*, 4090−4099.
(53) Boccaccini, A. R.; Cho, J.; Roether, J. A.; Thomas, B. J. C.; Minay, E. J.; Shaffer, M. S. P. *Carbon* **2006**, *44*, 3149−3160.
(54) Chicatun, F.; Cho, J.; Schaab, S.; Brusatin, G.; Colombo, P.; Roether, J.; Boccaccini, A. *Adv. Appl. Ceram.* **2007**, *106*, 186−195.
(55) Wu, M. S.; Huang, C. Y.; Lin, K. H. *Electrochem. Solid-State Lett.* **2009**, *12*, A129−A131.
(56) Du, C.; Pan, N. *J. Power Sources* **2006**, *160*, 1487−1494.
(57) Du, C.; Pan, N. *Nanotechnology* **2006**, *17*, 5314−5318.
(58) *Standard F756−00: Standard Practice for Assessment of Hemolytic Properties of Materials*; Technical Report from ASTM International:West Conshohocken, PA, 2000.
(59) Jia, L.; Shen, J.; Li, Z.; Zhang, D.; Zhang, Q.; Liu, G.; Zheng, D.; Tian, X. *Int. J. Pharm.* **2013**, *445*, 12−19.